JOURNAL OF THE MECHANICAL BEHAVIOR OF BIOMEDICAL MATERIALS 29 (2014) 529–543

Available online at www.sciencedirect.com

ScienceDirect

www.elsevier.com/locate/jmbbm

Editorial

Growing matter: A review of growth in living systems

ARTICLE INFO

Keywords:
Biomechanics
Continuum mechanics
Finite elements
Growth
Remodeling
Available online 28 October 2013

ABSTRACT

Living systems can grow, develop, adapt, and evolve. These phenomena are non-intuitive to traditional engineers and often difficult to understand. Yet, classical engineering tools can provide valuable insight into the mechanisms of growth in health and disease. Within the past decade, the concept of incompatible configurations has evolved as a powerful tool to model growing systems within the framework of nonlinear continuum mechanics. However, there is still a substantial disconnect between the individual disciplines, which explore the phenomenon of growth from different angles. Here we show that the nonlinear field theories of mechanics provide a unified concept to model finite growth by means of a single tensorial internal variable, the second order growth tensor. We review the literature and categorize existing growth models by means of two criteria: the microstructural appearance of growth, either isotropic or anisotropic; and the microenvironmental cues that drive the growth process, either chemical or mechanical. We demonstrate that this generic concept is applicable to a broad range of phenomena such as growing arteries, growing tumors, growing skin, growing airway walls, growing heart valve leaflets, growing skeletal muscle, growing plant stems, growing heart valve annuli, and growing cardiac muscle. The proposed approach has important biological and clinical applications in atherosclerosis, in-stent restenosis, tumor invasion, tissue expansion, chronic bronchitis, mitral regurgitation, limb lengthening, tendon tear, plant physiology, dilated and hypertrophic cardiomyopathy, and heart failure. Understanding the mechanisms of growth in these chronic conditions may open new avenues in medical device design and personalized medicine to surgically or pharmacologically manipulate development and alter, control, or revert disease progression.

1. Motivation

Growth is a distinguishing feature of all living things. Throughout the past century, the growth of living systems has fascinated plant physiologists, biologists, clinical scientists, mathematicians, physicists, computer scientists, and engineers alike (Taber, 1995). An intriguing feature of growth is the interplay of form and function, or, more specifically, the ability of the growing system to manipulate its microenvironment and, vice versa, the ability of the microenvironment to manipulate the microstructural architecture of growth (Ambrosi et al., 2011). The former is typically associated with growth-induced instabilities and growth-induced stresses, or, in a more abstract sense, with characterizing the impact of biology on the mechanics of the system (Li et al., 2012). The latter is associated with exploring the mechanisms that cause the system to grow, stretch, strain, or stress, or, abstractly, with understanding how mechanics can drive the biology of the system (Menzel and Kuhl, 2012). In the literature, these classifications go hand in hand with the notions of biomechanics and mechanobiology.

The first type of phenomena, growth-induced microenvironmental changes, has been studied intensely in plant physiology (Atkinson, 1900; Vandiver and Goriely, 2009), applied mathematics (Dervaux and Ben Amar, 2011; Goriely and BenAmar, 2007), and theoretical mechanics (Cai et al., 2010; Jin et al., 2011), and is now recognized to benefit from computational modeling in various clinical applications. Fig. 1 shows an example of growth-induced microenvironmental changes in a female red-eared slider turtle (Minnesota Department of Natural Resources, 2013). The turtle was found wearing a plastic six-pack ring around its shell. At the time of

Fig. 1 – Growth-induced microenvironmental changes in a nine-year old female red-eared slider turtle trapped in a plastic six-pack ring. At the time of capture, the turtle had worn the ring for five years. During this time, the ring had constrained the growth of the outer shell and created growth-induced stresses on the inner organs. X-ray imaging revealed that, except for the shell and the lung, all organs had grown and developed normally; adopted from Minnesota Department of Natural Resources (2013).

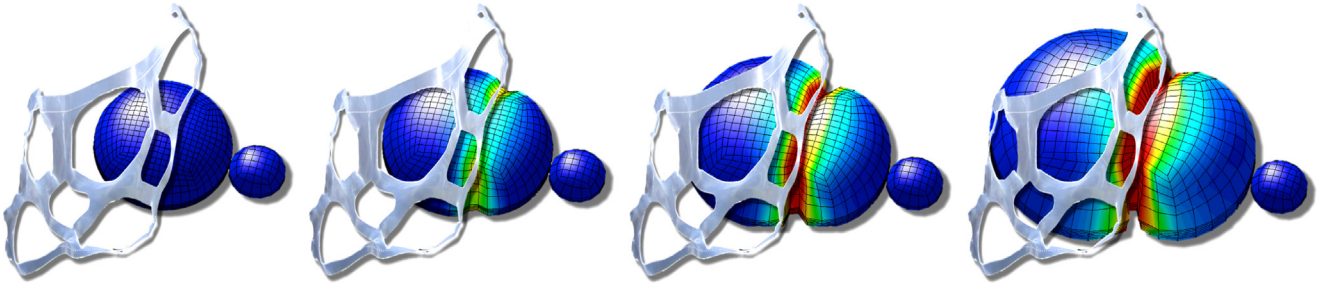

Fig. 2 – Growth-induced microenvironmental changes in a model turtle trapped in a plastic six-pack ring. The plastic ring constrains the growth of the shell and triggers growth-induced instabilities, which result in buckling and folding of the outer shell. Red regions close to the plastic ring are high-stress regions of constrained growth; blue regions away from the ring are stress-free regions of unconstrained growth. (For interpretation of the references to color in this figure caption, the reader is referred to the web version of this article.)

capture, the turtle was a nine years old and had worn the ring for approximately five years. During this time, the ring had constrained the growth of the outer shell and created growth-induced stresses on the inner organs. Fortunately, X-ray imaging revealed that all organs, except for the shell and the lung, were able to grow and develop normally. Fig. 2 illustrates a finite element simulation of the growing turtle. Constraining the deformation during growth triggers growth-induced instabilities, which result in buckling and folding of the outer shell (Cai et al., 2012). The red regions close to the ring are exposed to constrained growth and experience growth-induced stresses. The blue regions away from the ring can grow unboundedly and are stress free. Finite element simulations have the potential to predict the formation of growth-induced instabilities and identify regions of growth-induced stresses (Papastavrou et al., 2013). Computational modeling of growth might have immediate clinical implications in tumor growth during cancer (Narayanan et al., 2010), airway wall remodeling during asthma and chronic bronchitis (Moulton and Goriely, 2011), cortical folding during brain development (Bayly et al., this issue), crypt formation (Nelson et al., 2011), and gut looping during organogenesis (Savin et al., 2011). Beyond applications in developmental biology, understanding the morphogenesis and origin of shape may have broad applications in the natural sciences such as gap growth in dynamical systems (van den Bedem, 2001), mineral growth in geology (Kuhl and Schmid, 2007), or rock folding in tectonophysics (Jager et al., 2008).

The second type of phenomena, mechanically induced microstructural changes, has been studied in various types of soft tissues throughout the past decade. The crucial question here is not so much how growth induces instabilities or stress, but rather what it is that drives the growth process (Menzel and Kuhl, 2012). Research in this field has identified close correlations between the nature of the mechanical driving forces and the microstructural appearance of growth (Menzel, 2005). For example, it seems intuitive to hypothesize that volume growth, growth that is identical in all three directions in space, is driven by an isotropic mechanism such as the pressure (Himpel et al., 2005). Indeed, high blood pressure, or in clinical terms, hypertension, is a chronic condition that manifests itself in thickened arterial walls and thickened heart muscle (Kuhl et al., 2007). Similarly, we can postulate that area growth, growth that takes place in a particular plane of interest, is driven by a planar mechanism such as the area stretch (Socci et al., 2007). And indeed, plastic surgeons artificially create microenvironments with a controlled elevated area stretch to grow extra skin for defect repair (Buganza Tepole et al., 2011). Finally, it seems natural to assume that longitudinal growth, growth that takes place along a particular direction, is controlled by a unidirectional mechanism such as the fiber stretch (Barnett et al., 1980). A typical example is the controlled longitudinal growth of muscle fibers in clinical procedures such as limb lengthening (Zöllner et al., 2012). In all these cases, finite element simulations may play a crucial role in predicting, manipulating, and possibly reverting the natural progression of growth. This could have immediate applications in hypertension (Rausch et al., 2011), in-stent restenosis (Kuhl et al., 2007),

tissue expansion (Pamplona et al., this issue), mitral regurgitation (Timek et al., 2006), limb lengthening (Zöllner et al., 2012), tendon tear (Zumstein et al., 2012), myopia (Grytz et al., 2012), glaucoma (Grytz et al., 2012), and heart failure (Göktepe et al., 2010). Beyond applications in chronic disease, understanding the controlled manipulation of microstructural architecture could stimulate the design of smart materials with low stiffness and high responsiveness to mechanical cues with possible applications in therapeutics, metrology, sensors, microfluidics, and tissue engineering.

Table 1 illustrates selected examples of finite growth categorized by the microstructural type of growth and by the microenvironmental cues that drive the growth process. The first column addresses the first type of phenomena, growth-induced microenvironmental changes, which are primarily driven by chemical cues such as nutrients, hormones, or growth factors. The second column addresses the second type of phenomena, mechanically-induced microstructural changes, which are primarily driven by mechanical cues such as stress, strain, or stretch. Depending on the microstructural architecture of the system, both cues may initiate volume, area, or fiber growth as indicated in the individual rows.

To systematically compare the individual phenomena of growth, we briefly summarize the mathematical modeling of growth within the nonlinear field theories of mechanics in Section 2. We then specify the three different microstructural types of growth, volume growth, area growth, and fiber growth in Sections 3–5. For each type, we discuss selected examples of chemically-driven growth in Sections 3.1, 4.1, and 5.1, and of mechanically driven growth in Sections 3.2, 4.2, and 5.2. For illustrational purposes, we also add two diagnostic examples of pathological area growth and fiber growth in Sections 4.3 and 5.3 and demonstrate an example of combined growth in Section 6. We conclude with a discussion of the opportunities and challenges in modeling growth of living systems in Section 7.

Table 1 – Examples of growing matter categorized by the microstructural type of growth and by the microenvironmental cues that drive the growth process.

Microenvironment Microstructure	Chemical cues	Mechanical cues
Volume growth	**Tumors** *Nutrient-driven* Ductal carcinoma, tumor spheroids (Ambrosi and Mollica, 2002; Ciarletta et al., 2013; Narayanan et al., 2010)	**Arteries** *Stress-driven* Hypertension, restenosis (Bennett, 2003; Kuhl et al., 2007; Menzel, 2007; Taber and Humphrey, 2001; Waffenschmidt and Menzel, this issue)
	Fruit *Hormone-driven* Fruit growth (Böl et al., this issue)	
Area growth	**Lungs** *Growth-factor-driven* Asthma, chronic bronchitis (Jin et al., 2011; Li et al., 2011; Moulton and Goriely, 2011; Xie et al., this issue)	**Skin** *Strain-driven* Tissue expansion (Beauchenne et al., 1989; Buganza Tepole et al., 2011; De Filippo and Atala, 2002; Pamplona et al., this issue; Socci et al., 2007; Zöllner et al., 2012)
	Brain *Growth-factor-driven* Brain development, cortical folding (Bayly et al., this issue; Wyczalkowski et al., 2012; Xu et al., this issue)	**Heart valves** *Strain-driven* Mitral regurgitation (Chaput et al., 2008; Dal-Bianco et al., 2009; Grande-Allen et al., 2005; Rausch et al., 2012; Timek et al., 2006)
	Intestine *Growth-factor-driven* Intestinal villi, crypt formation (Balbi and Ciarletta, 2013; Nelson et al., 2011)	**Heart** *Stress-driven* Cardiac hypertrophy (Göktepe et al., 2010, 2010; Kroon et al., 2009; Rausch et al., 2011)
Fiber growth	**Plants** *Hormone-driven* Plant physiology (Atkinson, 1900; Holland et al., 2013; Vandiver and Goriely, 2009)	**Muscle** *Stretch-driven* Limb lengthening, tendon tear (Barnett et al., 1980; Caiozzo et al., 2002; Williams and Goldspink, 1978; Zöllner et al., 2012)
	Gut *Growth-factor-driven* Gut looping, organogenesis (Savin et al., 2011; Wyczalkowski et al., 2012)	**Eye** *Stretch-driven* Myopia, glaucoma (Grytz et al., 2012, 2012, this issue)
		Heart *Stretch-driven* Cardiac dilation, heart failure (Göktepe et al., 2010; Kerckhoffs et al., 2012; Klepach et al., 2012; Taber, 1995)

2. Continuum modeling of growth

Before discussing the individual examples of growing matter, we briefly summarize the continuum modeling of finite growth. In general, growth of a living system is associated with an increase in mass (Epstein and Maugin, 2000; Kuhl and Steinmann, 2003). Most living systems are multiphase materials that consist of a solid and one or more fluid phases (Humphrey and Rajagopal, 2003). Within the context of continuum mechanics, growth of multiphase materials is nothing but the exchange of mass between the fluid and the solid phases (Harper et al., this issue; Myers and Ateshian, this issue). Since the fluid phases are typically difficult to characterize and play a minor role in the mechanical characterization, simplified models characterize growth exclusively through an increase in solid mass, or, more precisely, through the kinematic changes associated with the increase in solid volume (Garikipati, 2009; Rodriguez et al., 1994). Here, for illustrational purposes, we restrict ourselves to kinematic changes of growing bodies with a single microstructural direction $\boldsymbol{n}_0$ (Göktepe et al., 2010).

We characterize the motion of these growing bodies through the deformation $\boldsymbol{\varphi}$, which maps material points $\boldsymbol{X}$ onto spatial points $\boldsymbol{x}=\boldsymbol{\varphi}(\boldsymbol{X},t)$ at any given time t. The key kinematic quantity in finite growth is the deformation gradient $\boldsymbol{F}$, which we decompose multiplicatively (Lee, 1969; Lubarda, 2004) into a reversible elastic part $\boldsymbol{F}^{\mathrm{e}}$ and an irreversible growth part $\boldsymbol{F}^{\mathrm{g}}$,

$$\boldsymbol{F}=\nabla_{\boldsymbol{X}}\boldsymbol{\varphi}=\boldsymbol{F}^{\mathrm{e}}\cdot\boldsymbol{F}^{\mathrm{g}}. \tag{1}$$

Here, $\nabla\{\circ\}=\partial_{\boldsymbol{X}}\{\circ\}|_t$ denotes the gradient of a field $\{\circ\}(\boldsymbol{X},t)$ with respect to the material position $\boldsymbol{X}$ at fixed time t. As illustrated in Fig. 3, we can interpret this multiplicative decomposition as a sequence of mappings from the reference configuration $\mathcal{B}_0$, via an incompatible growth configuration, to the current configuration $\mathcal{B}_t$. The Jacobian J defines the total change in volume, which we decompose multiplicatively into a reversible elastic volume change $J^{\mathrm{e}}=\det(\boldsymbol{F}^{\mathrm{e}})$ and an irreversible grown volume change $J^{\mathrm{g}}=\det(\boldsymbol{F}^{\mathrm{g}})$,

$$J=\det(\boldsymbol{F})=J^{\mathrm{e}}J^{\mathrm{g}}. \tag{2}$$

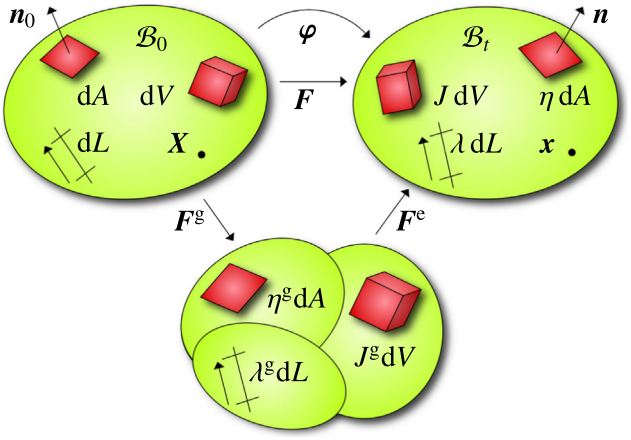

Fig. 3 – Kinematics of finite growth. Multiplicative decomposition of the deformation gradient into elastic and growth parts, $\boldsymbol{F}=\boldsymbol{F}^{\mathrm{e}}\cdot\boldsymbol{F}^{\mathrm{g}}$, and associated mappings of line elements, λ and λ^{g}, of area elements, η and η^{g}, and of volume elements, J and J^{g}.

Nanson's formula defines the total change in surface area η, which we decompose into a reversible elastic area change η^{e} and an irreversible grown area change $\eta^{\mathrm{g}}=\|J^{\mathrm{g}}\boldsymbol{F}^{\mathrm{g}-\mathrm{t}}\cdot\boldsymbol{n}_0\|$,

$$\eta=\|J\boldsymbol{F}^{-\mathrm{t}}\cdot\boldsymbol{n}_0\|=\eta^{\mathrm{e}}\eta^{\mathrm{g}}. \tag{3}$$

Here, $\boldsymbol{n}_0$ denotes the unit surface normal in the reference configuration. Last, we can decompose the stretch λ, the total change in length along the microstructural direction $\boldsymbol{n}_0$, into a reversible elastic strech λ^{e} and an irreversible growth stretch $\lambda^{\mathrm{g}}=\|\boldsymbol{F}^{\mathrm{g}}\cdot\boldsymbol{n}_0\|$,

$$\lambda=\|\boldsymbol{F}\cdot\boldsymbol{n}_0\|=\lambda^{\mathrm{e}}\lambda^{\mathrm{g}}. \tag{4}$$

We further introduce the right Cauchy–Green deformation tensor $\boldsymbol{C}$ and its elastic counterpart $\boldsymbol{C}^{\mathrm{e}}$,

$$\boldsymbol{C}=\boldsymbol{F}^{\mathrm{t}}\cdot\boldsymbol{F}=\boldsymbol{F}^{\mathrm{gt}}\cdot\boldsymbol{C}^{\mathrm{e}}\cdot\boldsymbol{F}^{\mathrm{g}}\quad\text{with}\quad\boldsymbol{C}^{\mathrm{e}}=\boldsymbol{F}^{\mathrm{et}}\cdot\boldsymbol{F}^{\mathrm{e}}, \tag{5}$$

along with the left Cauchy–Green deformation tensor $\boldsymbol{b}$ and its elastic counterpart $\boldsymbol{b}^{\mathrm{e}}$,

$$\boldsymbol{b}=\boldsymbol{F}\cdot\boldsymbol{F}^{\mathrm{t}}\quad\text{and}\quad\boldsymbol{b}^{\mathrm{e}}=\boldsymbol{F}^{\mathrm{e}}\cdot\boldsymbol{F}^{\mathrm{et}}. \tag{6}$$

It proves convenient to also introduce the growth deformation tensor, $\boldsymbol{C}^{\mathrm{g}}=\boldsymbol{F}^{\mathrm{gt}}\cdot\boldsymbol{F}^{\mathrm{g}}$, and its inverse $\boldsymbol{C}^{\mathrm{g}-1}$, which follows directly from the covariant pullback of the elastic left Cauchy–Green deformation tensor $\boldsymbol{b}^{\mathrm{e}}$,

$$\boldsymbol{C}^{\mathrm{g}-1}=\boldsymbol{F}^{\mathrm{g}-1}\cdot\boldsymbol{F}^{\mathrm{g}-\mathrm{t}}=\boldsymbol{F}^{-1}\cdot\boldsymbol{b}^{\mathrm{e}}\cdot\boldsymbol{F}^{-\mathrm{t}}. \tag{7}$$

In what follows, we characterize the material through two kinematic invariants,

$$J^{\mathrm{e}}=\det(\boldsymbol{F}^{\mathrm{e}})\quad\text{and}\quad I_1^{\mathrm{e}}=\boldsymbol{C}^{\mathrm{e}}:\boldsymbol{I}=\boldsymbol{b}^{\mathrm{e}}:\boldsymbol{I}, \tag{8}$$

with derivatives $\partial J^{\mathrm{e}}/\partial\boldsymbol{C}^{\mathrm{e}}=\frac{1}{2}J^{\mathrm{e}}\boldsymbol{C}^{\mathrm{e}-1}$ and $\partial I_1^{\mathrm{e}}/\partial\boldsymbol{C}^{\mathrm{e}}=\boldsymbol{I}$. On the smaller time scales of seconds, minutes, or hours, many living systems display a pronounced viscoelastic response. On the larger time scales of weeks or months, which are relevant to biological growth, it seems justified to neglect viscous effects and approximate the constitutive response as purely hyperelastic. Here we consider an isotropic hyperelastic material characterized through the Helmholtz free energy function,

$$\psi=\tfrac{1}{2}\lambda\ln^2(J^{\mathrm{e}})+\tfrac{1}{2}\mu[I_1^{\mathrm{e}}-3-2\ln(J^{\mathrm{e}})], \tag{9}$$

which defines the elastic Piola–Kirchhoff stress associated with the incompatible grown configuration,

$$\boldsymbol{S}^{\mathrm{e}}=2\frac{\partial\psi}{\partial\boldsymbol{C}^{\mathrm{e}}}=[\lambda\ln(J^{\mathrm{e}})-\mu]\boldsymbol{C}^{\mathrm{e}-1}+\mu\boldsymbol{I}. \tag{10}$$

Through a contravariant pull back to the reference configuration, we obtain the total Piola–Kirchhoff stress,

$$\boldsymbol{S}=\boldsymbol{F}^{\mathrm{g}-1}\cdot\boldsymbol{S}^{\mathrm{e}}\cdot\boldsymbol{F}^{\mathrm{g}-\mathrm{t}}=[\lambda\ln(J^{\mathrm{e}})-\mu]\boldsymbol{C}^{-1}+\mu\boldsymbol{C}^{\mathrm{g}-1}. \tag{11}$$

Through a contravariant push forward to the current configuration, we obtain the Kirchhoff stress,

$$\boldsymbol{\tau}=\boldsymbol{F}^{\mathrm{e}}\cdot\boldsymbol{S}^{\mathrm{e}}\cdot\boldsymbol{F}^{\mathrm{et}}=[\lambda\ln(J^{\mathrm{e}})-\mu]\boldsymbol{I}+\mu\boldsymbol{b}^{\mathrm{e}}. \tag{12}$$

To close the set of constitutive equations, it remains to specify the format of the growth tensor $\boldsymbol{F}^{\mathrm{g}}$ and the driving force for growth. In the following sections, we illustrate different growth tensors and possible driving forces by means of typical examples of volume growth, area growth, and fiber growth.

3. Volume growth

Volume growth is the simplest type of finite growth, for which the amount of growth is identical in all directions (Chen and Hoger, 2000). Its growth tensor is simply the identity tensor $\boldsymbol{I}$ scaled by a scalar-valued growth multiplier $\vartheta^{1/3}$,

$$\boldsymbol{F}^{g} = \vartheta^{1/3}\boldsymbol{I} \quad \text{where} \quad \vartheta = J^{g}. \tag{13}$$

In volume growth, the growth multiplier ϑ takes the interpretation of the grown volume J^{g}. We can directly invert the growth tensor,

$$\boldsymbol{F}^{g-1} = \vartheta^{-1/3}\boldsymbol{I}, \tag{14}$$

and obtain an explicit representation of elastic tensor,

$$\boldsymbol{F}^{e} = \vartheta^{-1/3}\boldsymbol{F}. \tag{15}$$

From this explicit expression, we can immediately calculate the elastic Jacobian,

$$J^{e} = J/\vartheta, \tag{16}$$

and the elastic left Cauchy Green tensor,

$$\boldsymbol{b}^{e} = \vartheta^{-2/3}\boldsymbol{b}. \tag{17}$$

to evaluate the Kirchhoff stress $\boldsymbol{\tau}$ according to Eq. (12). In the following subsections, we specify the evolution equation for the growth multiplier ϑ for two different types of volume growth, tumor growth and arterial growth.

3.1. Nutrient-driven volume growth of tumors

In tumors, growth is typically not controlled by mechanical driving forces such as stress or strain, but rather by biochemical driving forces such as nutrient supply (Araujo and McElwain, 2004). The nutrient concentration n typically displays regional variations across the tissue, larger outside and smaller inside the tumor (Ciarletta et al., 2012). This induces heterogeneous growth. To explore the mechanisms of nutrition-controlled growth, we propose the following simple exponential evolution equation for the growth multiplier (Ambrosi and Mollica, 2002),

$$\dot{\vartheta} = \frac{1}{\tau}\left[\vartheta^{\max} - 1\right]\left[\exp(-t/\tau)\right]\frac{1}{n}\langle n - n^{\text{crit}}\rangle,$$

where the first term controls unbounded exponential growth and the second term $\langle n - n^{\text{crit}}\rangle/n$ is the Heaviside step function, which is unity when the nutrient concentration n exceeds the critical threshold n^{crit} and zero otherwise. Here, for illustrative purposes, we assume that there is sufficient nutrient supply throughout the tissue, $n > n^{\text{crit}}$, such that growth is essentially homogeneous (Ciarletta et al., 2012). Because of this simplification, we can integrate the growth equation explicitly as $\vartheta = 1 + [\vartheta^{\max} - 1][1 - \exp(-t/\tau)]$. Three material parameters govern the growth process, the growth speed τ, the maximum volume growth $\vartheta^{\max}$ towards which the growth multiplier ϑ converges with progressing time t, and the nutrition threshold n^{crit} beyond which growth occurs (Ambrosi and Mollica, 2002).

Fig. 4 illustrates the mechanism of nutrient-driven volume growth of tumors by means of growing muffins. Similar to tumors, muffins typically grow isotropically (Narayanan et al., 2010). While tumors grow homogeneously once the nutrient concentration exceeds the nutrition threshold, muffins grow homogeneously once the baking temperature exceeds a critical temperature. At the lateral wall, where growth is constrained, growth induces high stress concentrations shown in red. At the top, were growth is unconstrained, the body is stress free shown in blue. This boundary value problem mimics the early development of ductal carcinoma in situ, the initial phase of growth in breast cancer (Ambrosi and Mollica, 2002). At this stage, the growing tumor is non-invasive since it is spatially confined inside the cylindrical breast duct. However, it induces significantly elevated wall stresses, similar to the ones we observe in the muffin wall (Ciarletta et al., 2012). Here, for illustrative purposes, we have selected a homogeneous growth model. In reality, tumor growth is heterogeneous, controlled by regionally varying nutrient concentrations (Ambrosi and Mollica, 2002) or, more precisely, by a combination of regionally varying nutrient concentrations and growth-inhibiting stresses (Ambrosi and Mollica, 2004). Supplemented by controlled experiments, computational modeling of tumor growth could help to explain how local nutrient and stress concentrations can drive tumor invasion (Araujo and McElwain, 2004). Understanding how biochemical and biomechanical forces can manipulate mechanotransduction pathways in growing multicellular spheroids would be a major step towards novel therapeutic treatments for various different types of cancer (Ciarletta et al., 2013).

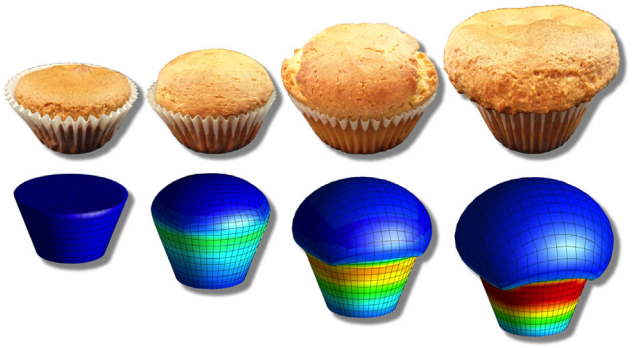

Fig. 4 – Nutrient-driven volume growth of tumors. Similar to tumors, the muffins shown here grow isotropically. While tumors grow homogeneously once the nutrient concentration exceeds the nutrition threshold, muffins grow homogeneously once the baking temperature exceeds a critical temperature. Red regions at the sides are high-stress regions of constrained growth; blue regions at the top are stress-free regions of unconstrained growth. (For interpretation of the references to color in this figure caption, the reader is referred to the web version of this article.)

3.2. Stress-driven volume growth of arteries

In cardiovascular tissue, growth is typically driven by hypertension, a major risk factor in myocardial infarction, heart failure, and aneurysms (Taber and Humphrey, 2001). Hypertension is a chronic medical condition associated with elevated blood pressure. It thus seems reasonable to consider

growth as a stress-driven process governed by the pressure p. A possible evolution equation for stress-driven volume growth could take the following format (Himpel et al., 2005),

$$\dot{\vartheta} = \frac{1}{\tau}\left[\frac{\vartheta^{\max}-\vartheta}{\vartheta^{\max}-1}\right]^{\gamma}\langle p - p^{\text{crit}}\rangle \quad \text{with} \quad p = \text{tr}(\boldsymbol{\tau}),$$

where the first term controls unbounded growth and the second term in the Macaulay brackets represents a stress-driven growth criterion similar to the yield function in the theory of plasticity. In this simplified model, four material parameters govern the growth process, the growth speed τ, the shape parameter for the growth curve γ, the maximum volume growth $\vartheta^{\max}$, and the physiological pressure level p^{crit} beyond which growth occurs (Lubarda and Hoger, 2002).

Fig. 5 illustrates a typical example of stress-driven volume growth in response to arterial stenting (Kuhl et al., 2007). To widen the narrowed lumen of an atherosclerotic artery, vascular surgeons stent the artery by implanting a small metal-meshed tube. The forces that keep the tube in place create elevated wall stresses, which induce mechanotransduction pathways that ultimately cause the artery to grow. This phenomenon is referred to as in-stent restenosis (Bennett, 2003). In the red regions close to the stent, the arterial wall has doubled its initial wall volume to sustain the elevated wall stress. In the unstented blue regions, the wall volume remains unchanged. Here, for illustrative purposes, we have selected isotropic constitutive models for both the elastic arterial wall and its growth. In reality, arterial growth and remodeling are complex anisotropic, multiphase phenomena, which are elaborated in detail in Roccabianca et al. (this issue) and Waffenschmidt and Menzel (this issue) of this special issue. Understanding the progression of arterial growth in response to elevated wall stresses is critical to prevent disease and improve treatment options. For example, drug-eluting stents have been proposed to manipulate the mechanotransduction pathways in response to stenting with the goal to suppress undesired wall thickening (Bennett, 2003). Mathematical modeling and computational simulations could help to optimize stent shapes, stent coating, stent placement, and stent timing (Mortier et al., 2010).

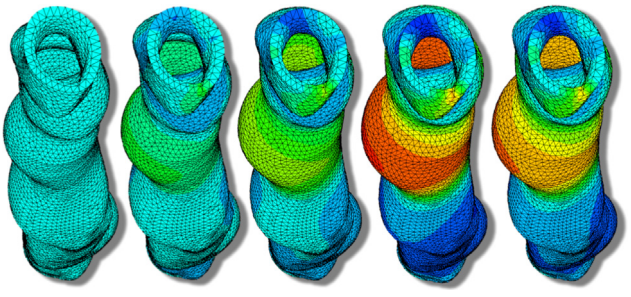

Fig. 5 – Stress-driven volume growth of arteries. Atherosclerotic arteries are stented to widen their lumen. The forces of the stent create elevated wall stresses, which cause the artery to grow, a phenomenon known as in-stent restenosis. In red regions, the arterial wall has doubled its volume; in blue regions, the wall volume remains unchanged. (For interpretation of the references to color in this figure caption, the reader is referred to the web version of this article.)

4. Area growth

Area growth is a type of finite growth, for which growth is isotropic in a plane characterized through the unit normal $\boldsymbol{n}_0$, while there is no growth in the out-of-plane direction (Buganza Tepole et al., 2011),

$$\boldsymbol{F}^{\text{g}} = \sqrt{\vartheta}\boldsymbol{I} + [1-\sqrt{\vartheta}]\boldsymbol{n}_0 \otimes \boldsymbol{n}_0 \quad \text{where} \quad \vartheta = \eta^{\text{g}}. \tag{18}$$

In area growth, the growth multiplier ϑ takes the interpretation of the grown surface area η^{g}. Since there is no growth in the normal direction, the amount of area growth is identical to the total amount of volume growth, $J^{\text{g}} = \vartheta$. The growth tensor for area growth has a simple rank-one update structure and we can invert it directly using the Sherman–Morrison formula,

$$\boldsymbol{F}^{\text{g}-1} = \frac{1}{\sqrt{\vartheta}}\boldsymbol{I} + \left[1-\frac{1}{\sqrt{\vartheta}}\right]\boldsymbol{n}_0 \otimes \boldsymbol{n}_0, \tag{19}$$

to obtain the an explicit representation of elastic tensor,

$$\boldsymbol{F}^{\text{e}} = \frac{1}{\sqrt{\vartheta}}\boldsymbol{F} + \left[1-\frac{1}{\sqrt{\vartheta}}\right]\boldsymbol{n} \otimes \boldsymbol{n}_0. \tag{20}$$

Here $\boldsymbol{n} = \boldsymbol{F}\cdot\boldsymbol{n}_0$ denotes the spatial normal as illustrated in Fig. 3. To evaluate the Kirchhoff stress $\boldsymbol{\tau}$ according to Eq. (12), we calculate the elastic Jacobian,

$$J^{\text{e}} = J/\vartheta, \tag{21}$$

and the elastic left Cauchy–Green tensor,

$$\boldsymbol{b}^{\text{e}} = \frac{1}{\vartheta}\boldsymbol{b} + \left[1-\frac{1}{\vartheta}\right]\boldsymbol{n} \otimes \boldsymbol{n}. \tag{22}$$

In the following subsections, we specify the evolution equation for the growth multiplier ϑ for three different types of area growth, airway wall growth, skin growth, and heart valve leaflet growth.

4.1. *Growth-factor-driven area growth of airway walls*

In chronic obstructive pulmonary disease, growth is primarily controlled by biochemical driving forces such as growth factor concentrations (Moulton and Goriely, 2011). Here, we propose the following simple exponential evolution equation for the growth multiplier (Papastavrou et al., 2013),

$$\dot{\vartheta} = \frac{1}{\tau}\left[\vartheta^{\max}-1\right]\left[\exp\left(-t/\tau\right)\right]\frac{1}{g}\langle g - g^{\text{crit}}\rangle.$$

The first term controls unbounded exponential growth and the second term, $\langle g-g^{\text{crit}}\rangle/g$, is the Heaviside step function. The Heaviside function is unity when the concentration of growth factors g exceeds the critical threshold g^{crit} and is zero otherwise. For simplicity, we assume that the growth factor concentration is larger than this threshold throughout the entire airway wall, $g > g^{\text{crit}}$. This implies that growth is homogeneous, and we can explicitly integrate the growth equation in time to obtain the following explicit expression $\vartheta = 1 + [\vartheta^{\max}-1][1-\exp(-t/\tau)]$. Here, τcharacterizes the speed of growth and $\vartheta^{\max}$ limits the maximum amount of growth towards which the growth multiplier ϑ converges with progressing time t.

Fig. 6 illustrates area growth of the mucous membrane, the inner layer of the airway wall (Papastavrou et al., 2013). Once the growth factor concentration exceeds a critical threshold, the

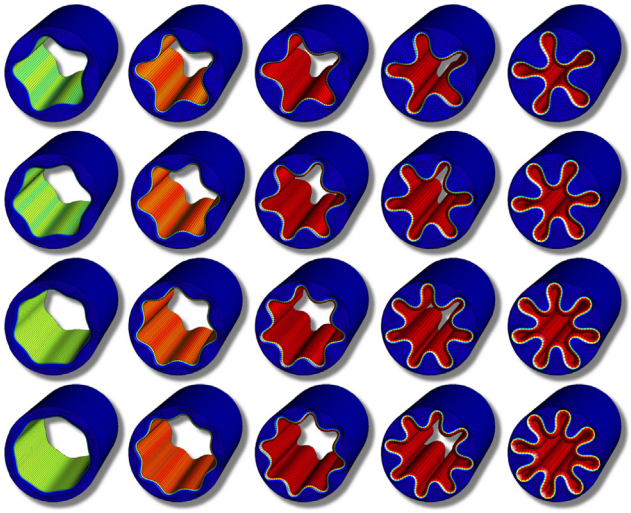

Fig. 6 – Growth-factor-driven area growth of airway walls. The inner layer, the mucous membrane, grows homogeneously once the growth factor concentration exceeds a critical threshold, while the outer layer does not grow. Red regions at the inner wall are regions of high growth-induced deviatoric stress; blue regions at the outer wall are non-growing and almost stress-free. (For interpretation of the references to color in this figure caption, the reader is referred to the web version of this article.)

inner layer grows homogeneously, while the outer layer does not grow (Li et al., 2011). In the red regions, membrane growth induces folding associated with local stress concentrations (Wiggs et al., 1997). In the blue regions, the airway wall is non-growing and almost stress-free. Here, we have modeled the mucous membrane as a truly three-dimensional material volume. For phenomena like airway wall remodeling, in which the growing layer is significantly thinner than the remaining non-growing tissue, recent studies suggest to model the membrane as a growing two-dimensional material surface equipped with its own potential energy (Papastavrou et al., 2013). To trigger the formation of folds, we have introduced five, six, seven, and eight infinitesimal perturbations. One of the contributions of this special issue elaborates the critical number of folds in airway wall remodeling using energetic considerations (Xie et al., this issue). The computational modeling of area growth has immediate biomedical applications in the diagnosis and treatment of asthma, gastritis, and obstructive sleep apnoea (Moulton and Goriely, 2011). Beyond biomedical applications, the scientific understanding of growth-induced morphological instabilities and surface wrinkling has important implications in material sciences, manufacturing, and microfabrication, with applications in soft lithography, metrology, and flexible electronics (Li et al., 2012).

4.2. *Strain-driven area growth of skin*

In skin, growth is primarily driven by mechanical strain (De Filippo and Atala, 2002). Tissue expansion capitalizes on this phenomenon and induces controlled overstretch to create new skin for local defect repair in plastic and reconstructive surgery (Baker, 1991). A possible evolution equation for strain-driven area growth of skin could take the following format (Buganza Tepole et al., 2011),

$$\dot{\vartheta} = \frac{1}{\tau}\left[\frac{\vartheta^{\max}-\vartheta}{\vartheta^{\max}-1}\right]^{\gamma}\langle \eta^{e}-\eta^{crit}\rangle \quad \text{with} \quad \eta^{e}=\frac{\|JF^{-t}\cdot n_0\|}{\vartheta}.$$

The first term controls unbounded growth and the second term in the Macaulay brackets represents a strain-driven growth criterion similar to the damage loading function in continuum damage mechanics (Socci et al., 2007). Four material parameters govern the growth process, the growth speed τ, the shape parameter for the growth curve γ, the maximum area growth ϑ^{max}, and the physiological area stretch η^{crit} beyond which growth occurs (Zöllner et al., 2012).

Fig. 7 illustrates a typical example of strain-driven area growth of skin (Buganza Tepole et al., 2011). Upon tissue expansion, expanders of different shapes, spherical, square, rectangular, and crescent-shaped, are subcutaneously implanted and gradually inflated (van Rappard et al., 1988). The elevated strain causes the skin to grow. In the center of the expanded region shown in red, the area stretch is highest and skin gradually triples its initial area. In the periphery shown in blue, the area stretch is close to zero and the skin area remains unchanged (Buganza Tepole et al., 2012). These regional variations in skin growth agree nicely with experimental observations of controlled skin growth in rodents (Beauchenne et al., 1989).

Fig. 8 illustrates the clinical example of strain-driven area growth in plastic and reconstructive surgery (Gosain et al., 2009). In this example of pediatric forehead reconstruction, three tissue expanders are subcutaneously implanted and gradually inflated to create skin flaps for defect repair in situ (Zöllner et al., in press). Over a period of multiple weeks, the increased strain causes skin to grow (Rivera et al., 2005). In the center of the expanded regions shown in red, the area stretch is highest and skin triples its initial areal. In the

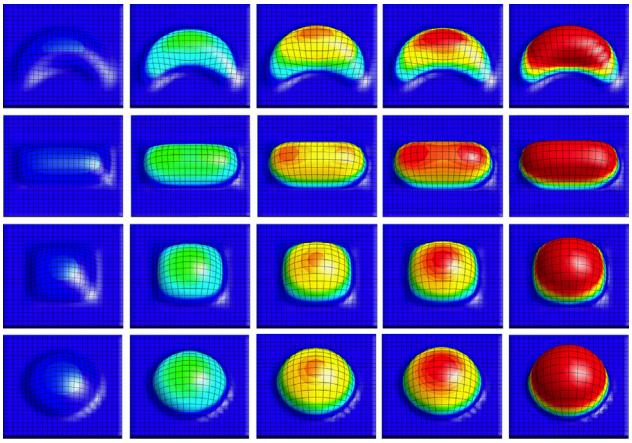

Fig. 7 – Strain-driven area growth of skin. Upon tissue expansion, spherical, square, rectangular, and crescent-shaped expanders are subcutaneously implanted and gradually inflated. The controlled over-stretch causes skin to grow. In red regions, skin has tripled its area; in blue regions, skin area remains unchanged. (For interpretation of the references to color in this figure caption, the reader is referred to the web version of this article.)

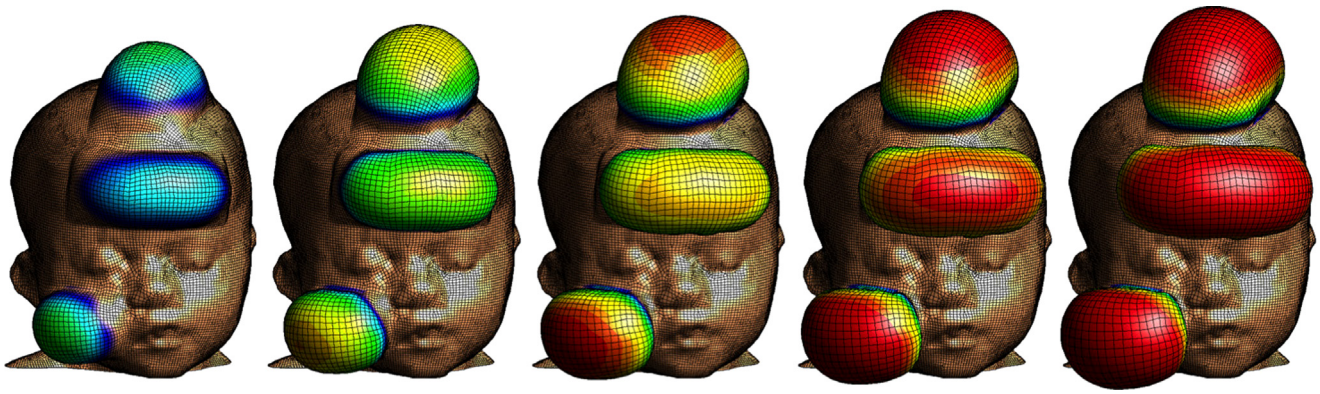

Fig. 8 – Strain-driven area growth of skin. In pediatric forehead reconstruction, tissue expanders are subcutaneously implanted and gradually inflated for defect repair in situ. The controlled over-stretch causes skin to grow. In red regions, skin has tripled its area; in blue regions, skin area remains unchanged. (For interpretation of the references to color in this figure caption, the reader is referred to the web version of this article.)

periphery shown in blue, the area stretch is close to zero and the skin area remains unchanged (Zöllner et al., 2012). For simplicity, we have selected an isotropic constitutive model for the baseline elastic response of skin. In reality, skin is incompressible (Pamplona and Carvalho, 2012) and anisotropic (Buganza Tepole et al., 2012), and its growth is closely associated with other phenomena such as capillary network formation (Ciarletta and Ben Amar, 2012). One of the contributions of this special issue illustrates the potential of computational simulations in skin expansion (Pamplona et al., this issue). Computational models for skin growth could serve as valuable tools to rationalize clinical process parameters such as expander geometry, expander size, filling volume, filling pressure, and inflation timing to minimize tissue necrosis and maximize patient comfort in plastic and reconstructive surgery (Zöllner et al., in press).

4.3. *Pathological area growth of heart valve leaflets*

In mitral regurgitation, the heart valves no longer seal properly (Yiu et al., 2000). If untreated, mitral regurgitation can become life threatening, since it is associated with a severe back flow and a gradual increase in work load. Only recently, heart valve leaflets in diseased individuals were found to be significantly larger than those in normal patients (Chaput et al., 2008). This motivates the hypothesis that leaflets can chronically adapt in response to microenvironmental changes and increase their area to close properly and prevent back flow (Dal-Bianco et al., 2009). While it is not entirely clear, whether leaflet growth is primarily driven by biochemical or biomechanical factors (Grande-Allen et al., 2005), characterizing the amount of growth in an in vivo setting might provide valuable insight into the mechanisms of leaflet growth. To quantify the amount of surface area growth in response to myocardial infarction, controlled experiments were performed in five sheep (Rausch et al., 2012). Leaflet coordinates before and after infarction were reconstructed from implanted markers using bi-plane videofluoroscopy (Rausch et al., 2011). From these leaflet coordinates, we can quantify the amount of infarct-induced area growth,

$$\eta^{g} = \| J^{g} \boldsymbol{F}^{g-t} \cdot \boldsymbol{n}_0 \| ,$$

and the amount of infarct-induced growth along the circumferential and radial directions $\boldsymbol{n}_{cc}$ and $\boldsymbol{n}_{rr}$,

$$\lambda^{g}_{cc} = \| \boldsymbol{F}^{g} \cdot \boldsymbol{n}_{cc} \| \quad \text{and} \quad \lambda^{g}_{rr} = \| \boldsymbol{F}^{g} \cdot \boldsymbol{n}_{rr} \| .$$

For simplicity, this characterization assumes that the elastic deformation between the baseline state and the chronically grown state is negligible, $\boldsymbol{F}^{e} \doteq \boldsymbol{I}$, such that the measured deformation between both states can be attributed exclusively to pathological leaflet growth, $\boldsymbol{F}^{g} = \boldsymbol{F}$.

Fig. 9 illustrates the pathological area growth of heart valve leaflets in chronic ischemic cardiomyopathy (Rausch et al., 2012). The first row displays the initial leaflet geometry of five animals. The second, third, and fourth rows illustrate the amount of area growth η^{g}, circumferential growth λ^{g}_{cc}, and radial growth λ^{g}_{rr}. In the red regions, the leaflets grow by +30% in area and by +10% in length. In the blue regions, the leaflets shrink by −30% in area and by −10% in length. The average leaflet surface area increases by 16% (Rausch et al., 2012). The phenomenon of adaptive leaflet growth was confirmed by three other studies, which reported a radial leaflet lengthening (Timek et al., 2006), and an increase in leaflet area (Chaput et al., 2009; Dal-Bianco et al., 2009). This study demonstrates that mechanical stretch, induced by annular dilation and papillary muscle tethering, can trigger leaflet growth. While this study is primarily diagnostic with a focus on quantifying changes in leaflet area, another study in this special issue focusses on quantifying changes in leaflets microstructure in response to microenvironmental changes (Soares et al., this issue). Understanding the mechanisms of leaflet adaptation may open new avenues in pharmacology or surgery to manipulate mechanotransduction pathways with a goal to increase leaflet area and reduce the degree of regurgitation (Gillam, 2008; Rausch and Kuhl, 2013).

5. Fiber growth

Fiber growth is a type of finite growth, for which growth takes place exclusively along the fiber direction $\boldsymbol{n}_0$, while there is no growth in the cross-fiber direction (Zöllner et al., in press),

$$\boldsymbol{F}^{g} = \boldsymbol{I} + [\vartheta - 1]\, \boldsymbol{n}_0 \otimes \boldsymbol{n}_0 \quad \text{where} \quad \vartheta = \lambda^{g}. \tag{23}$$

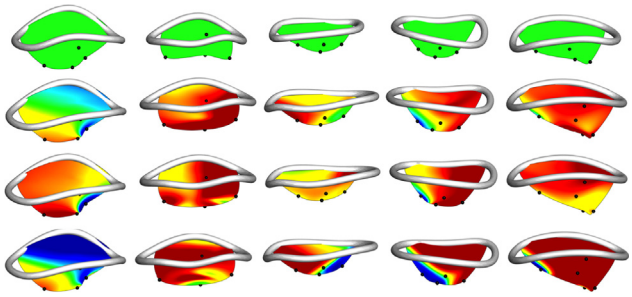

Fig. 9 – Pathological area growth of heart valve leaflets. Implanted videofluoroscopic markers reveal heterogeneous and anisotropic changes in leaflet area in chronic ischemic cardiomyopathy. Initial leaflets of five ischemic sheep (first row), and their growth in area (second row), growth in circumferential direction (third row), and growth in radial direction (fourth row) demonstrate regional and directional variations. In red regions leaflets grow by +30% in area and by +10% length; in blue regions leaflets shrink by −30% in area and by −10% in length. (For interpretation of the references to color in this figure caption, the reader is referred to the web version of this article.)

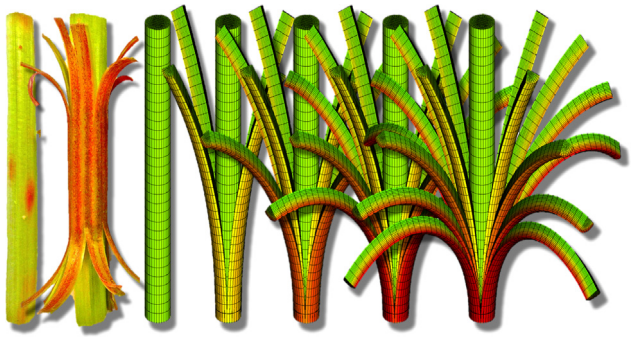

Fig. 10 – Hormone-driven fiber growth of plant stems. The epidermal cells of the outer surface grow slower than the parenchyma cells of the inner core. Differential growth creates a state of longitudinal tissue tension. The balanced interplay between surface tension, shown in red, and bulk compression, shown in green, gives the stem its characteristic rigidity. When the surface layers are peeled off, they contract and bend outward, while the inner core expands as tissue tension is released. (For interpretation of the references to color in this figure caption, the reader is referred to the web version of this article.)

In fiber growth, the growth multiplier ϑ takes the interpretation of the chronic fiber lengthening λ^g. Since there is no cross-fiber growth, this fiber lengthening is identical to the total amount of volume growth, $J^g = \vartheta$. The growth tensor has a simple rank-one update structure and we can invert it directly using the Shermann–Morrison formula,

$$\boldsymbol{F}^{g\,-1} = \boldsymbol{I} + \left[\frac{1}{\vartheta} - 1\right] \boldsymbol{n}_0 \otimes \boldsymbol{n}_0, \tag{24}$$

to obtain an explicit representation of the elastic tensor,

$$\boldsymbol{F}^e = \boldsymbol{F} + \left[\frac{1}{\vartheta} - 1\right] \boldsymbol{n} \otimes \boldsymbol{n}_0. \tag{25}$$

This expression allows us to evaluate the Kirchhoff stress $\boldsymbol{\tau}$ according to Eq. (12), by means of the elastic Jacobian,

$$J^e = J/\vartheta, \tag{26}$$

and the elastic left Cauchy–Green tensor,

$$\boldsymbol{b}^e = \boldsymbol{b} + \left[\frac{1}{\vartheta^2} - 1\right] \boldsymbol{n} \otimes \boldsymbol{n}. \tag{27}$$

In the following subsections, we specify the evolution equation for the growth multiplier ϑ for three different types of fiber growth, plant stem growth, skeletal muscle growth, and heart valve annulus growth.

5.1. *Hormone-driven fiber growth of plant stems*

In plant stems, growth is primarily controlled by biochemical driving forces such as plant hormones (Thimann and Schneider, 1938). Typical examples are auxin or gibberellins. We propose the following simple exponential evolution for hormone controlled plant growth (Holland et al., 2013):

$$\dot{\vartheta} = \frac{1}{\tau}\left[\vartheta^{\max} - 1\right]\left[\exp\left(-t/\tau\right)\right]\frac{1}{h}\langle h - h^{\text{crit}}\rangle.$$

The first term controls unbounded exponential growth and the second term, $\langle h - h^{\text{crit}}\rangle/h$, is the Heaviside step function, which is unity when the hormone concentration h exceeds the critical threshold h^{crit} and zero otherwise. To initiate homogeneous growth, we assume that the hormone concentration is larger than this threshold throughout the entire plant stem, $h > h^{\text{crit}}$. We can then explicitly integrate the growth equation in time to obtain the following explicit expression $\vartheta = 1 + [\vartheta^{\max} - 1][1 - \exp(-t/\tau)]$. Here, τcharacterizes the speed of growth and $\vartheta^{\max}$ is maximum stem lengthening towards which the growth multiplier ϑ converges with progressing time t.

Fig. 10 illustrates the phenomenon of hormone-driven fiber growth of a rhubarb stem (Holland et al., 2013). During plant growth, the densely packed, brick-shaped epidermal cells of the outer surface shown in red grow slower than the thin-walled parenchyma cells of the inner core shown in green. Differential growth creates a state of longitudinal tissue tension or residual stress (Atkinson, 1900). The balanced interplay between surface tension and bulk compression gives the stem its characteristic rigidity (Gager, 1916). When the surface layers are peeled off, they contract and bend outward, while the inner core expands as tissue tension is released (Goldstein and Goriely, 2006). In plant physiology, the petiole of rhubarb serves as a widely used model system to visualize and quantify the effects of growth of thin surface layers (Vandiver and Goriely, 2009). While stem growth is typically unidirectional, growth of fruit as discussed in one of the contributions of this special issue (Böl et al., this issue), can be a truly tridirectional phenomenon. Thin film phenomena as discussed here are inherent to applications in material sciences, manufacturing, and microfabrication (Li et al., 2012). Modeling of growing thin films such as the epithelial layer can provide insight into the complex interplay between thin films and the bulk (Nelson et al., 2011), which might be particularly valuable when

designing novel functionalized surfaces with distinct user-defined properties (Holland et al., 2013).

5.2. Stretch-driven fiber growth of skeletal muscle

In skeletal muscle, longitudinal growth is primarily driven by mechanical stretch (Barnett et al., 1980). Typical applications are controlled muscle growth in limb lengthening, tendon lengthening, tendon transfer, and tendon reattachment after tendon tear. A possible evolution equation for stretch-driven longitudinal fiber growth of skeletal muscle could take the following format (Zöllner et al., 2012),

$$\dot{\vartheta} = \frac{1}{\tau}\left[\frac{\vartheta^{\max}-\vartheta}{\vartheta^{\max}-1}\right]^{\gamma}\langle \lambda^{e}-\lambda^{crit}\rangle \quad \text{with} \quad \lambda^{e}=\frac{\|\boldsymbol{F}\cdot\boldsymbol{n}_0\|}{\vartheta}.$$

The first term controls unbounded growth and the second term in the Macaulay brackets represents a stretch-driven growth criterion. The growth process is governed by four material parameters, the growth speed τ, the shape parameter for the growth curve γ, the maximum fiber lengthening $\vartheta^{\max}$, and the physiological stretch limit λ^{crit} beyond which growth occurs.

Fig. 11 illustrates fiber growth of skeletal muscle in a retracted biceps brachii muscle after tendon tear (Zöllner et al., 2012). To surgically reattach the torn tendon, the shortened, retracted muscle needs to re-lengthen. Muscle re-lengthening can be induced by applying controlled chronic over-stretch (Zumstein et al., 2012). When stretched beyond the physiological limit, skeletal muscles responds through sarcomerogenesis (Caiozzo et al., 2002), the creation and serial deposition of new sarcomere units, to gradually lengthen and return to its optimal operating range (Williams and Goldspink, 1978). Proximally, at the shoulder side, where the muscle-tendon interface is relatively sharp, the muscle lengthens by 14% and more, shown in red. Distally, at the elbow side, where the stiff tendon branches into the soft muscle tissue, the muscle lengthens by 4% and less, shown in blue. Regional variations in muscle stretch, shorter close to and longer away from the muscle-tendon interface, are caused by the stiff tendon, which locally enhances the resistance to stretch (Goldspink, 1968). Modeling the time sequence of muscle lengthening may help surgeons to prevent muscle overstretch and make informed decisions about optimal stretch increments, stretch timing, and stretch amplitudes in controlled limb and tendon lengthening (Gerber et al., 2009).

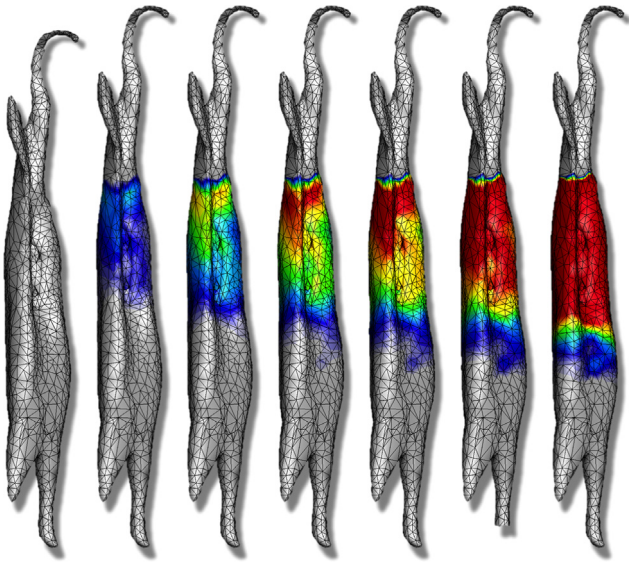

Fig. 11 – Stretch-driven fiber growth of skeletal muscle. To reattach a torn tendon, the retracted and shortened biceps brachii muscle is gradually re-lengthened. Chronic over-stretch causes the muscle to grow. In red regions, the muscle has increased its length by 14%; in blue regions, muscle length remains unchanged. (For interpretation of the references to color in this figure caption, the reader is referred to the web version of this article.)

5.3. Pathological fiber growth of heart valve annuli

In mitral regurgitation, the heart valve dilates and pulls the leaflets apart to no longer seal the valve properly (Levine et al., 2002). A common repair technique is to implant a tight ring around the heart valve annulus to bring the leaflets back together (Bothe et al., 2012). Fig. 12 displays an annuloplasty ring designed specifically for patients with chronic ischemic mitral regurgitation (Daimon et al., 2005). While it is not clear to date whether annular dilation in these patients is primarily driven by biochemical or biomechanical factors, characterizing the amount of growth in an in vivo setting might provide valuable insight into the mechanisms of annular growth. To quantify the amount of fiber growth and annular dilation, controlled experiments were performed in nine sheep (Tibayan et al., 2003). Annular coordinates of healthy and dilated annuli were reconstructed from implanted markers before infarction and five weeks after infarction using biplane videofluoroscopy. From these coordinates, we can quantify the infarct-induced annular stretch as the relative change in tangent vector length (Rausch et al., 2012),

$$\lambda^{g} = \|\mathrm{d}_s\mathbf{c}\| / \|\mathrm{d}_s\mathbf{c}_0\|.$$

Here, $\mathbf{c}_0$ and $\mathbf{c}$ denote the parametric representation of the healthy and dilated annulus. Their derivatives with respect to

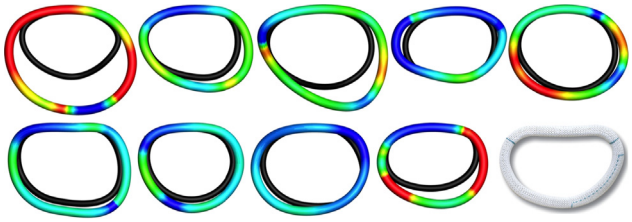

Fig. 12 – Pathological fiber growth of heart valve annuli. Implanted videofluoroscopic markers reveal heterogeneous annular dilation in chronic ischemic cardiomyopathy. Healthy annuli of nine sheep underlaid in black and their grown counterparts overlaid in color demonstrate significant regional variations in growth. In red regions, annuli lengthened up to 40%; in blue regions, annuli remained unchanged. Implanting annuloplasty rings (bottom right) can help to re-establish the healthy baseline state. (For interpretation of the references to color in this figure caption, the reader is referred to the web version of this article.)

the arc length s define the corresponding tangent vectors $d_s\mathbf{c}_0$ and $d_s\mathbf{c}$. For simplicity, the study assumes that the elastic annulus stretch between the healthy and dilated states is negligible, $\lambda^e = 1$, such that the measured deformation between both states can be attributed exclusively to pathological annular dilation, $\lambda^g = \lambda$.

Fig. 12 illustrates the pathological annular lengthening in chronic ischemic cardiomyopathy (Rausch et al., 2013). The underlaid black contours show the healthy annuli of nine sheep. The overlaid colorcoded contours characterize chronic annular dilation. In the red regions, the annuli lengthen up to 40%. In the blue regions, the annuli remain unchanged. Implanting annuloplasty rings, as shown on the bottom right, can help to re-narrow the valvular lumen and re-establish the healthy baseline state (Carpentier et al., 2010). The challenge in modern annuloplasty is to restore a physiological annular configuration while preserving native annular dynamics (Cosgrove et al., 1995). The pronounced heterogeneity in annular dilation suggests that this can be best achieved through individualized rings with regionally varying stiffnesses (Rausch et al., 2012). While this study is primarily diagnostic with a focus on quantifying the kinematics of annular dilation, a recent study focusses on quantifying the dynamics associated with growing rings (Moulton et al., 2013). Computational modeling of annular dilation can play a crucial role in the rational design of novel smart annuloplasty devices. More importantly, it may provide mechanistic insight to establish surgical guidelines for personalized device selection (Rausch et al., 2013).

6. Combined growth

Combined fiber and cross-fiber growth is a type of growth, for which growth may take place along the fiber direction $\boldsymbol{n}_0$ and in the plane orthogonal to it (Göktepe et al., 2010),

$$\mathbf{F}^g = \sqrt{\vartheta^\perp}\,\mathbf{I} + \left[\vartheta^\parallel - \sqrt{\vartheta^\perp}\right]\boldsymbol{n}_0 \otimes \boldsymbol{n}_0 \quad \text{where} \quad \begin{matrix}\vartheta^\perp = \eta^g \\ \vartheta^\parallel = \lambda^g.\end{matrix} \tag{28}$$

To model this combined type of growth, we introduce two independent growth multipliers, the cross-fiber growth as the change in area $\vartheta^\perp = \eta^g$ and the fiber growth as the change in length $\vartheta^\parallel = \lambda^g$. This implies that the total amount of volume growth is equal to the product of the two, $J^g = \vartheta^\perp \vartheta^\parallel$. Although the growth tensor looks slightly more complex than in the previous sections, it has preserved its rank-one update structure for its explicit inversion,

$$\mathbf{F}^{g-1} = \frac{1}{\sqrt{\vartheta^\perp}}\boldsymbol{I} + \left[\frac{1}{\vartheta^\parallel} - \frac{1}{\sqrt{\vartheta^\perp}}\right]\boldsymbol{n}_0 \otimes \boldsymbol{n}_0. \tag{29}$$

which provides an explicit representation of elastic tensor,

$$\mathbf{F}^e = \frac{1}{\sqrt{\vartheta^\perp}}\boldsymbol{F} + \left[\frac{1}{\vartheta^\parallel} - \frac{1}{\sqrt{\vartheta^\perp}}\right]\boldsymbol{n} \otimes \boldsymbol{n}_0. \tag{30}$$

To evaluate the Kirchhoff stress according to Eq. (12), we determine the elastic Jacobian,

$$J^e = J/[\vartheta^\parallel \vartheta^\perp], \tag{31}$$

and the elastic left Cauchy–Green tensor,

$$\boldsymbol{b}^e = \frac{1}{\vartheta^\perp}\boldsymbol{b} + \left[\frac{1}{\vartheta^{\parallel 2}} - \frac{1}{\vartheta^\perp}\right]\boldsymbol{n} \otimes \boldsymbol{n}. \tag{32}$$

In the following subsection, we specify the evolution equations for the growth multipliers $\vartheta^\perp$ and $\vartheta^\parallel$ for the case of cardiac growth.

6.1. Stretch- and stress-driven fiber and cross-fiber growth of cardiac muscle

In cardiac muscle, fiber growth is primarily driven by mechanical stretch, while fiber thickening is driven by mechanical stress (Opie et al., 2006). The former is associated with volume-overload induced cardiac dilation, while the latter is associated with pressure-overload induced wall thickening (Hunter and Chien, 1999). We suggest the following evolution equations for fiber and cross-fiber growth (Göktepe et al., 2010),

$$\dot{\vartheta}^\perp = \frac{1}{\tau^\perp}\left[\frac{\vartheta^{\perp\max} - \vartheta}{\vartheta^{\perp\max} - 1}\right]^{\gamma^\perp} \langle p - p^{\text{crit}}\rangle \quad \text{with } p = \text{tr}(\boldsymbol{\tau})$$

$$\dot{\vartheta}^\parallel = \frac{1}{\tau^\parallel}\left[\frac{\vartheta^{\parallel\max} - \vartheta}{\vartheta^{\parallel\max} - 1}\right]^{\gamma^\parallel} \langle \lambda^e - \lambda^{\text{crit}}\rangle \quad \text{with } \lambda^e = \frac{\|\boldsymbol{F}\cdot\boldsymbol{n}_0\|}{\vartheta}.$$

The first terms control unbounded growth and the second terms in the Macaulay brackets represent pressure- and stretch-driven growth criteria. Both growth processes are governed by a total of eight material parameters, the growth speeds $\tau^\perp$ and $\tau^\parallel$, the shape parameters $\gamma^\perp$ and $\gamma^\parallel$, the maximum fiber and cross-fiber growth $\vartheta^{\perp\max}$ and $\vartheta^{\parallel\max}$, and the physiological growth limits $\vartheta^{\perp\text{crit}}$ and $\vartheta^{\parallel\text{crit}}$ beyond which growth occurs.

Fig. 13 illustrates the effects of stretch- and stress-driven fiber and cross-fiber growth of cardiac muscle (Göktepe et al., 2010). The top rows show how the wall of the heart thickens as the muscle fibers grow in cross-fiber direction in response to pressure overload or hypertension (Kumar et al., 2005). In the lateral wall of the left ventricle shown in red, the heart muscle fibers have increased their thickness by 200% causing the wall to thicken from 1 cm to 3 cm, while the right ventricle is virtually unaffected by hypertension (Rausch et al., 2011). The bottom rows show how the heart dilates as the muscle fibers grow along the fiber direction in response to volume overload or hyperstretch (Gerdes, 2002). In the equatorial regions of the left ventricle shown in red, the heart muscle fibers have lengthened by 50% causing the ventricle to dilate, while the apical and basal regions of the left ventricle and the entire right ventricle remain unaffected by volume overload (Göktepe et al., 2010). Here, for illustrational purposes, we have treated wall thickening and ventricular dilation as independent phenomena although experiments have demonstrated that both may occur simultaneously in cardiac disease (Tsamis et al., 2012). Early models approximate cardiac growth as plain isotropic (Kroon et al., 2009), while more advanced models treat both thickening and dilation in a single unified approach (Kerckhoffs et al., 2012). Growth of the heart is typically progressive and may lead to heart failure, a chronic condition for which there is currently no cure. Stem cells offer promising new therapies targeted at

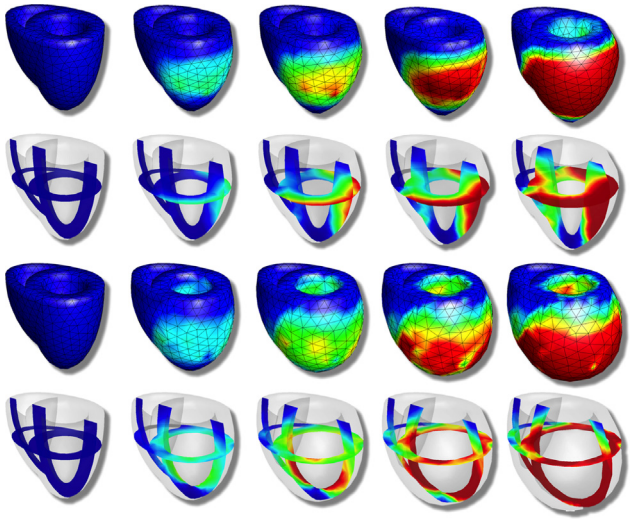

Fig. 13 – Stretch- and stress-driven fiber and cross-fiber growth of cardiac muscle. In response to pressure overload or hypertension, the wall of the heart thickens as the muscle fibers grow in cross-fiber direction (top). In response to volume overload or hyperstretch, the heart dilates as the muscle fibers grow along the fiber direction (bottom). In red regions, the heart muscle has increased its thickness by 200% (top) and its length by 50% (bottom); in blue regions the heart muscle remains unchanged. (For interpretation of the references to color in this figure caption, the reader is referred to the web version of this article.)

replacing the dysfunctional heart muscle with healthy, fully functional tissue. However, despite intense research, stem cell therapies are still associated with many unknowns. Computational modeling has the potential to identify required cell volumes, optimal injection sites, and most effective injection timing (Wenk et al., 2011). Computational modeling of cardiac growth can also be crucial to provide guidelines in more conservative surgical procedures such as surgical ventricular restoration (Klepach et al., 2012).

7. Discussion

Living systems can undergo a continuous turnover in response to microenvironmental cues. Alterations in these cues, in particular during development and disease, may cause the system to grow. Here we have illustrated the phenomenon of growth in arteries, tumors, lungs, plants, skin, muscle, and the heart. From a biological point of view, these types of growth are intrinsically different and entirely unrelated. From a mechanical point of view, however, they have a lot in common: They all fall within the same nonlinear field theories of mechanics, supplemented by the concept of incompatible configurations. Irrespective of the nature of growth, the incompatible configuration is uniquely defined in terms of a single tensorial internal variable, the second order growth tensor. Here we have reviewed different formats of the growth tensor and systematically categorized existing growth models by means of two criteria, the microstructural appearance of growth and the microenvironmental cues that drive the growth process.

We have introduced the generic mathematical backbone for growing systems and illustrated its computational realization. Computational modeling has the potential to provide mechanistic insight into the causes and effects of growth. It can uniquely integrate information from multiple length and time scales towards providing a holistic view of various phenomena in development and disease progression. Yet, despite intense efforts, computational modeling of growth is still in its infancy. While there is a general agreement on the underlying mathematical equations and their computational realization, an urgent need remains for more sophisticated experiments to calibrate and validate these models. To convert current reproductive models into truly predictive tools, we need controlled experiments that acquire quantitative biochemical and biomechanical information across multiple spatial scales at multiple points in time. Once calibrated and validated, growth models have immediate applications in biologically and clinically relevant fields such as atherosclerosis, in-stent restenosis, tumor invasion, tissue expansion, chronic bronchitis, mitral regurgitation, limb lengthening, tendon tear, plant physiology, dilated and hypertrophic cardiomyopathy, and heart failure. Understanding the fundamental mechanisms of growth in living systems is a challenging but rewarding task. It may inspire improved medical devices design and optimize personalized treatment options.

Acknowledgments

This study was supported by the National Science Foundation CAREER award CMMI 0952021, by the National Science Foundation INSPIRE grant 1233054, and by the National Institutes of Health grant U54 GM072970.

REFERENCES

Atkinson, G.F., 1900. Lessons in Botany. Henry Hold & Co, New York.
Ambrosi, D., Mollica, F., 2002. On the mechanics of a growing tumor. Int. J. Eng. Sci. 40, 1297–1316.
Ambrosi, D., Mollica, F., 2004. The role of stress in the growth of a multicell spheroid. J. Math. Biol. 48, 477–499.
Araujo, R.P., McElwain, D.L.S., 2004. A history of the study of solid tumor growth: the contribution of mathematical modelling. Bull. Math Biol. 66, 1039–1091.
Ambrosi, D., Ateshian, G.A., Arruda, E.M., Cowin, S.C., Dumais, J., Goriely, A., Holzapfel, G.A., Humphrey, J.D., Kemkemer, R., Kuhl, E., Olberding, J.E., Taber, L.A., Garikipati, K., 2011. Perspectives on biological growth and remodeling. J. Mech. Phys. Solids 59, 863–883.
Baker, S.R., 1991. Fundamentals of expanded tissue. Head Neck 13, 327–333.
Balbi, V., Ciarletta, P., 2013. Morpho-elasticity of intestinal villi. J. Roy. Soc. Interface 10, 2013109.
Barnett, J.G., Holly, R.G., Ashmore, C.R., 1980. Stretch-induced growth in chicken wing muscles: biochemical and morphological characterization. Am. J. Physiol. 239, C39–C46.
Bayly, P.V., Taber, L.A., Kroenke, C.D. Mechanical forces in cerebral cortical folding: a review of measurements and

models. J Mech Behavior Biomed Mat., http://dx.doi.org/10.1016/j.jmbbm.2013.02.018, this issue.
Beauchenne, J.G., Chambers, M.M., Peterson, A.E., Scott, P.G., 1989. Biochemical, biomechanical, and physical changes in the skin in an experimental animal model of therapeutic tissue expansion. J. Surg. Res. 47, 507–514.
Bennett, M.R., 2003. In-stent stenosis: pathology and implications for the development of drug eluting stents. Heart 89, 218–224.
Böl, M., Bolea Alberto, A. On a new model for inhomogeneous volume growth of elastic bodies. J Mech Behavior Biomed Mat., http://dx.doi.org/10.1016/j.jmbbm.2013.01.027, this issue.
Bothe, W., Rausch, M.K., Kvitting, J.P., Echtner, D.K., Walther, M., Ingels, N.B., Kuhl, E., Miller, D.C., 2012. How do annuloplasty rings affect mitral annular strains in the normal beating ovine heart?. Circulation 126, S231–S238.
Buganza Tepole, A., Ploch, C.J., Wong, J., Gosain, A.K., Kuhl, E., 2011. Growing skin: a computational model for skin expansion in reconstructive surgery. J. Mech. Phys. Solids 59, 2177–2190.
Buganza Tepole, A., Gosain, A.K., Kuhl, E., 2012. Stretching skin: the physiological limit and beyond. Int. J. Nonlin. Mech. 47, 938–949.
Cai, S., Bertoldi, K., Wang, H., Suo, Z., 2010. Osmotic collapse of a void in an elastomer: breathing, buckling and creasing. Soft Matter. 6, 5770–5777.
Cai, S., Chen, D., Suo, Z., Hayward, R.C., 2012. Creasing instability of elastomer films. Soft Matter. 8, 1301–1304.
Caiozzo, V.J., Utkan, A., Chou, R., Khalafi, A., Chandra, H., Baker, M., Rourke, B., Adams, G., Baldwin, K., Green, S., 2002. Effects of distraction on muscle length: mechanisms involved in sarcomerogenesis. Clin. Orthop. Rel. Res. 403S, S133–S145.
Carpentier, A.F., Adams, D.H., Filsoufi, F., 2010. Carpentier's Reconstructive Valve Surgery. Elsevier Saunders.
Chaput, M., Handschumacher, M.D., Tournoux, F., Hua, L., Guerrero, J.L., Vlahakes, G.J., Levine, R.A., 2008. Mitral leaflet adaptation to ventricular remodeling: occurrence and adequacy in patients with functional mitral regurgitation. Circulation 118, 845–852.
Chaput, M., Handschumacher, M.D., Guerrero, J.L., Holmvang, G., Dal-Bianco, J.P., Sullivan, S., Vlahakes, G.J., Hung, J., Levine, R.A., 2009. Mitral leaflet adaptation to ventricular remodeling: prospective changes in a model of ischemic mitral regurgitation. Circulation 120, S99–S103.
Chen, Y.C., Hoger, A., 2000. Constitutive functions of elastic materials in finite growth and deformation. J. Elast. 59, 175–193.
Ciarletta, P., Ben Amar, M., 2012. Papillary networks in the dermal-epidermal junction of skin: a biomechanical model. Mech. Res. Comm. 42, 68–76.
Ciarletta, P., Ambrosi, D., Maugin, G.A., 2012. Mass transport in morphgenetic processes: a second gradient theory for volumetric growth and material remodeling. J. Mech. Phys. Solids 60, 432–450.
Ciarletta, P., Ambrosi, D., Maugin, G.A., Preziosi, L., 2013. Mechano-transduction in tumor growth modelling. Eur. Phys. J. E. 36, 23.
Cosgrove, D.M., Arcidi, J.M., Rodriguez, L., Stewart, W.J., Powell, K., Thomas, J.D., 1995. Initial experience with the Cosgrove–Edwards Annuloplasty System. Ann. Thorac. Surg. 60, 499–503.
Daimon, M., Fukuda, S., Adams, D.H., McCarthy, P.M., Gillinov, A.M., Carpentier, A., Filsoufi, F., Abascal, V.M., Rigolin, V.H., Salzberg, S., Huskin, A., Langenfeld, M., Shiota, T., 2005. Mitral valve repair with Carpentier–McCarthy–Adams IMR ETlogix annuloplasty ring for ischemic mitral regurgitation. Circulation 114, I588–I593.
Dal-Bianco, J.P., Aikawa, E., Bischoff, J., Guerrero, J.L., Handschumacher, M.D., Sullivan, S., Johnson, B., Titus, J.S., Iwamoto, Y., Wylie-Sears, J., Levine, R.A., Carpentier, A., 2009. Active adaptation of the tethered mitral valve: insights into a compensatory mechanism for functional mitral regurgitation. Circulation 120, 334–342.
De Filippo, R.E., Atala, A., 2002. Stretch and growth: the molecular and physiologic influences of tissue expansion. Plast. Reconstr. Surg. 109, 2450–2462.
Dervaux, J., Ben Amar, M., 2011. Buckling considerations in constrained growth. J. Mech. Phys. Solids 59, 538–560.
Epstein, M., Maugin, G.A., 2000. Thermomechanics of volumetric growth in uniform bodies. Int. J. Plast. 16, 951–978.
Gager, C.S., 1916. Fundamentals of Botany. P. Blakiston's Son & Co, Philadelphia.
Garikipati, K., 2009. The kinematics of biological growth. Appl. Mech. Rev. 62 030801.1-030801.7.
Gerber, C., Meyer, D.C., Frey, E., von Rechenberg, B., Hoppeler, H., Frigg, R., Jost, B., Zumstein, M.A., 2009. Reversion of structural muscle changes caused by chronic rotator cuff tears using continuous musculotendinous traction. J. Shoulder Elb. Surg. 18, 163–171.
Gerdes, A.M., 2002. Cardiac myocyte remodeling in hypertrophy and progression to failure. J. Card. Fail. 8, S264–268.
Gillam, L.D., 2008. Is it time to update the definition of functional mitral regurgitation? Structural changes in the mitral leaflets with left ventricular dysfunction. Circulation 118, 797–799.
Goldstein, R.E., Goriely, A., 2006. Dynamic buckling of morphoelastic filaments. Phys. Rev. E 74, 010901.
Goldspink, G., 1968. Sarcomere length during post-natal growth of mammalian muscle fibers. J. Cell Sci. 3, 539–548.
Göktepe, S., Abilez, O.J., Kuhl, E., 2010. A generic approach towards finite growth with examples of athlete's heart, cardiac dilation, and cardiac wall thickening. J. Mech. Phys. Solids 58, 1661–1680.
Göktepe, S., Abilez, O.J., Parker, K.K., Kuhl, E., 2010. A multiscale model for eccentric and concentric cardiac growth through sarcomerogenesis. J. Theor. Biol. 265, 433–442.
Goriely, A., BenAmar, M., 2007. On the definition and modeling of incremental, cumulative, and continuous growth laws in morphoelasticity. Biomech. Mod. Mechanobiol. 6, 289–296.
Gosain, A.K., Zochowski, C.G., Cortes, W., 2009. Refinements of tissue expansion for pediatric forehead reconstruction a 13-year experience. Plast. Reconstr. Surg. 124, 1559–1570.
Grande-Allen, K.J., Borowski, A.G., Troughton, R.W., Houghtaling, P.L., DiPaola, N.R., Moravec, C.S., Vesely, I., Griffin, B.P., 2005. Apparently normal mitral valves in patients with heart failure demonstrate biochemical and structural derangements. J. Am. Coll. Cardiol. 45, 54–61.
Grytz, R., Sigal, I.A., Ruberti, J.W., Meschke, G., Crawford Downs, J., 2012. Lamina cribrosa thickening in early glaucoma predicted by a microstructure motivated growth and remodeling approach. Mech. Mat. 44, 99–109.
Grytz, R., Girkin, C.A., Libertiaux, V., Crawford Downs, J., 2012. Perspectives on biomechanical growth and remodeling mechanisms in glaucoma. Mech. Res. Comm. 42, 92–106.
Grytz, R., Fazio, M.A., Girard, M.J.A., Libertiaux, V., Bruno, L., Gardiner, S., Girkin, C.A., Downs, J.C., 2013. Material properties of the posterior human sclera. J. Mech. Behav. Biomed Mat., http://dx.doi.org/10.1016/j.jmbbm.2013.03.027, this issue.
Harper, J.L., Simon, B.R., Vande Geest, J.P., 2013. A one dimensional mixed porohyperelastic transport swelling finite element model with growth. J Mech Behavior Biomed Mat. this issue, http://dx.doi.org/10.1016/j.jmbbm.2013.04.019.
Himpel, G., Kuhl, E., Menzel, A., Steinmann, P., 2005. Computational modeling of isotropic multiplicative growth. Comput. Mod. Eng. Sci. 8, 119–134.
Holland, M.A., Kosmata, T., Goriely, A., Kuhl, E., 2013. On the mechanics of thin films and growing surfaces. Math. Mech. Solids 18, 561–575.
Humphrey, J.D., Rajagopal, K.R., 2003. A constrained mixture model for arterial adaptations to a sustained step change in blood flow. Biomech. Model Mechanobiol. 2, 109–126.

Hunter, J.J., Chien, K.R., 1999. Signaling pathways for cardiac hypertrophy and failure. New Eng. J. Med. 341, 1276–1283.
Jager, P., Schmalholz, S.M., Schmid, D.W., Kuhl, E., 2008. Brittle fracture during folding rocks – a finite element study. Philos. Mag. 88, 3245–3263.
Jin, L., Cai, S., Suo, Z., 2011. Creases in soft tissues generated by growth. EPL Front. Phys. 95 64002.1-64002.6.
Kerckhoffs, R., Omens, J., McCulloch, A.D., 2012. A single strain-based growth law predicts concentric and eccentric cardiac growth during pressure and volume overload. Mech. Res. Comm. 42, 40–50.
Klepach, D., Lee, L.C., Wenk, J.F., Ratcliffe, M.B., Zohdi, T.I., Navia, J.A., Kassab, G.S., Kuhl, E., Guccione, J.M., 2012. Growth and remodeling of the left ventricle: a case study of myocardial infarction and surgical ventricular restoration. Mech. Res. Comm. 42, 134–141.
Kroon, W., Delhaas, T., Arts, T., Bovendeerd, P., 2009. Computational modeling of volumetric soft tissue growth: application to the cardiac left ventricle. Biomech. Mod. Mechanobiol. 8, 301–309.
Kuhl, E., Steinmann, P., 2003. Mass- and volume specific views on thermodynamics for open systems. Proc. Roy. Soc. 459, 2547–2568.
Kuhl, E., Maas, R., Himpel, G., Menzel, A., 2007. Computational modeling of arterial wall growth: attempts towards patient specific simulations based on computer tomography. Biomech. Mod. Mechanobiol. 6, 321–331.
Kuhl, E., Schmid, D.W., 2007. Computational modeling of mineral unmixing and growth – an application of the Cahn–Hilliard equation. Comp. Mech. 39, 439–451.
Kumar, V., Abbas, A.K., Fausto, N., 2005. Robbins and Cotran Pathologic Basis of Disease. Elsevier Saunders.
Lee, E.H., 1969. Elastic-plastic deformation at finite strains. J. Appl. Mech. 36, 1–6.
Levine, R.A., Hung, J., Otsuji, Y., Messas, E., Liel-Cohen, N., Nathan, N., Handschumacher, M.D., Guerrero, J.L., He, S., Yoganathan, A.P., Vlahakes, G.J., 2002. Mechanistic insights into functional mitral regurgitation. Curr. Cardiol. Rep. 4, 125–129.
Li, B., Cao, Y.P., Feng, X.Q., Gao, H., 2011. Surface wrinkling of mucosa induced by volumetric growth: theory, simulation and experiment. J. Mech. Phys. Solids 59, 758–774.
Li, B., Cao, Y.P., Feng, X.Q., Gao, H., 2012. Mechanics of morphological instabilities and surface wrinkling in soft materials: a review. Soft Matter. 8, 5728–5745.
Lubarda, V.A., Hoger, A., 2002. On the mechanics of solids with a growing mass. Int. J. Solids Struct. 39, 4627–4664.
Lubarda, V.A., 2004. Constitutive theories based on the multiplicative decomposition of deformation gradient: thermoelasticity, elastoplasticity, and biomechanics. Appl. Mech. Rev. 57, 95–108.
Menzel, A., 2005. Modelling of anisotropic growth in biological tissues – a new approach and computational aspects. Biomech. Model. Mechanobiol. 3, 147–171.
Menzel, A., 2007. A fibre reorientation model for orthotropic multiplicative growth. Biomech. Model. Mechanobiol. 6, 303–320.
Menzel, A., Kuhl, E., 2012. Frontiers in growth and remodeling. Mech. Res. Comm. 42, 1–14.
Minnesota Department of Natural Resources. Peanut the Turtle. ⟨http://www.dnr.state.mn.us/adoptriver/peanut.html⟩, 2013.
Mortier, O., Holzapfel, G.A., De Beule, M., Van Loo, D., Taeymans, Y., Segers, P., Verdonck, P., Verhegghe, B., 2010. A novel simulation strategy for stent insertion and deployment in curved coronary bifurcations: comparison of three drug-eluting stents. Annu. Biomed. Eng. 38, 88–99.
Moulton, D.E., Goriely, A., 2011. Circumferential buckling instability of a growing cylindrical tube. J. Mech. Phys. Solids 59, 525–537.
Moulton, D.E., Goriely, A., 2011. Possible role of differential growth in airway wall remodeling in asthma. J. Appl. Physiol. 110, 1003–1012.
Moulton, D.E., Lessinnes, T., Goriely, A., 2013. Morphoelastic rots. Part I: a single growing elastic rod. J. Mech. Phys. Solids 61, 398–427.
Myers, K., Ateshian, G.A., 2013. Interstitial growth and remodeling of biological tissues: tissue composition as state variables. J. Mech. Behav. Biomed. Mat. http://dx.doi.org/10.1016/j.jmbbm.2013.03.003, this issue.
Narayanan, H., Verner, S.N., Mills, K.L., Kemkemer, R., Garikipati, K., 2010. In silica estimates of the free energy rates in growing tumor spheroids. J. Phys. Cond. Matter 22, 194122.
Nelson, M.R., Howard, D., Jensen, O.E., King, J.R., Rose, F.R.A.J., Waters, S.L., 2011. Growth-induced buckling of an epithelial layer. Biomech. Model. Mechanobiol. 10, 883–900.
Opie, L.H., Commerford, P.J., Gersh, B.J., Pfeffer, M.A., 2006. Controversies in ventricular remodelling. Lancet 367, 356–367.
Pamplona, D.C., Carvalho, C., 2012. Characterization of human skin through skin expansion. J. Mech. Mat. Struct. 7, 641–655.
Pamplona, D.C., Velloso, R.Q., Radwanski, H.N., 2013. On skin expansion. J. Mech. Behav. Biomed. Mat., http://dx.doi.org/10.1016/j.jmbbm.2013.03.023, this issue.
Papastavrou, A., Steinmann, P., Kuhl, E., 2013. On the mechanics of continua with boundary energies and growing surfaces. J. Mech. Phys. Solids 61, 1446–1463.
Rausch, M.K., Dam, A., Göktepe, S., Abilez, O.J., Kuhl, E., 2011. Computational modeling of growth: systemic and pulmonary hypertension in the heart. Biomech. Model. Mechanobiol. 10, 799–811.
Rausch, M.K., Bothe, W., Kvitting, J.P.E., Göktepe, S., Miller, D.C., Kuhl, E., 2011. In vivo dynamic strains of the ovine anterior mitral valve leaflet. J. Biomech. 44, 1149–1157.
Rausch, M.K., Tibayan, F.A., Miller, D.C., Kuhl, E., 2012. Evidence of adaptive mitral leaflet growth. J. Mech. Behav. Biomed. Mat. 15, 208–217.
Rausch, M.K., Bothe, W., Kvitting, J.P., Swanson, J.C., Miller, D.C., Kuhl, E., 2012. Mitral valve annuloplasty – a quantitative clinical and mechanical comparison of different annuloplasty devices. Ann. Biomed. Eng. 40, 750–761.
Rausch, M.K., Tibayan, F.A., Ingels, N.B., Miller, D.C., Kuhl, E., 2013. Mechanics of the mitral annulus in chronic ischemic cardiomyopathy. Ann. Biomed. Eng. 41, 2171–2180.
Rausch, M.K., Kuhl, E., 2013. On the effect of prestrain and residual stress in thin biological membranes. J. Mech. Phys. Solids 61, 1955–1969.
Rivera, R., LoGiudice, J., Gosain, A.K., 2005. Tissue expansion in pediatric patients. Clin. Plast. Surg. 32, 35–44.
Roccabianca, S., Figueroa, C.A., Tellides, G., Humphrey, J.D., 2013. Quantification of regional differences in aortic stiffness in the aging human. J. Mech. Behav. Biomed. Mat., http://dx.doi.org/10.1016/j.jmbbm.2013.01.026, this issue.
Rodriguez, E.K., Hoger, A., McCulloch, A.D., 1994. Stress-dependent finite growth in soft elastic tissues. J. Biomech. 27, 455–467.
Savin, T., Kurpios, N.A., shyer, A.E., Florescu, P., Liang, H., Mahadevan, L., Tabin, C.J., 2011. On the growth and form of the gut. Nature 476, 57–62.
Soares, A.L.F., van Geemen, D., van den Bogaerdt, A.J., Oomens, C.W.J., Bouten, C.V.C., Baaijens, F.P.T., 2013. Mechanics of the pulmonary valve in the aortic position. J. Mech. Behav. Biomed. Mat. http://dx.doi.org/10.1016/j.jmbbm.2013.07.009, this issue.
Socci, L., Pennati, G., Gervaso, F., Vena, P., 2007. An axisymmetric computational model of skin expansion and growth. Biomech. Model. Mechanobiol. 6, 177–188.
Taber, L.A., 1995. Biomechanics of growth, remodeling and morphogenesis. Appl. Mech. Rev. 48, 487–545.

Taber, L.A., Humphrey, J.D., 2001. Stress-modulated growth, residual stress, and vascular heterogeneity. J. Biomech. Eng. 123, 528–535.
Thimann, K.V., Schneider, C.L., 1938. Differential growth in plant tissues. Am. J. Bot. 25, 627–641.
Tibayan, F.A., Rodriguez, F., Langer, F., Zasio, M.K., Bailey, L., Liang, D., Daughters, G.T., Ingels, N.B., Miller, D.C., 2003. Annular remodeling in chronic ischemic mitral regurgitation: ring selection implications. Ann. Thorac. Surg. 76, 1549–1554.
Timek, T.A., Lai, D.T., Dagum, P., Liang, D., Daughters, G.T., Ingels, N.B., Miller, D.C., 2006. Mitral leaflet remodeling in dilated cardiomyopathy. Circulation 114, I518–I523.
Tsamis, A., Cheng, A., Nguyen, T.C., Langer, F., Miller, D.C., Kuhl, E., 2012. Kinematics of cardiac growth – in vivo characterization of growth tensors and strains. J. Mech. Behav. Biomed. Mat. 8, 165–177.
van den Bedem, H., 2001. Statistical properties of hyperbolic systems with tangential singularities. Nonlinearity 14, 1393–1410.
Vandiver, R., Goriely, A., 2009. Differential growth and residual stress in cylindrical elastic structures. Philos. Trans. R. Soc A 367, 3607–3630.
van Rappard, J.H.A., Molenaar, J., van Doorn, K., Sonneveld, G.J., Borghouts, J.M.H.M., 1988. Surface-area increase in tissue expansion. Plast. Reconstr. Surg. 82, 833–839.
Waffenschmidt, T., Menzel, A., 2013. Extremal states of energy of a double-layered thick-walled tube – application to residually stressed arteries. J. Mech. Behav. Biomed. Mat., http://dx.doi.org/10.1016/j.jmbbm.2013.05.023, this issue.
Wenk, J.F., Eslami, P., Zhang, Z., Xu, C., Kuhl, E., Gorman, J.H., Robb, J.D., Ratcliffe, M.B., Gorman, R.C., Guccione, J.M., 2011. A novel method for quantifying the in-vivo mechanical effect of material injected into a myocardial infarction. Ann. Thorac. Surg. 92, 935–941.
Wiggs, B.R., Hrousis, C.A., Drazen, J.M., Kamm, R.D., 1997. On the mechanism of mucosal folding in normal and asthmatic airways. J. Appl. Physiol. 83, 1814–1821.
Williams, P.E., Goldspink, G., 1978. Changes in sarcomere lengths and physiological properties in immobilized muscle. J. Anat. 127, 459–468.
Wyczalkowski, M.A., Chen, Z., Filas, B.A., Varner, V.D., Taber, L.A., 2012. Computational models for mechanics of morphogenesis. Birth Defects Res. C 96, 132–152.
Xie, B.L., Cao, Y.P., Feng, X.Q., 2013. Effects of internal pressure and surface tension on the growth-induced wrinkling of mucosae. J. Mech. Behavior. Biomed. Mat., http://dx.doi.org/10.1016/j.jmbbm.2013.05.009, this issue.
Xu, G., Knutsen, A.K., Dikranian, K., Kroenke, C.D., Bayly, P.V., Tabler, L.A., 2010. Axons pull on the brain, but tension does not drive cortical folding. J. Biomech. Eng. 132, 071013.
Yiu, S.F., Enriquez-Sarano, M., Tribouilloy, C., Seward, J.B., Tajik, A.J., 2000. Determinants of the degree of functional mitral regurgitation in patients with systolic left ventricular dysfunction: a quantitative clinical study. Circulation 102, 1400–1406.
Zöllner, A.M., Buganza Tepole, A., Kuhl, E., 2012. On the biomechanics and mechanobiology of growing skin. J. Theor. Biol. 297, 166–175.
Zöllner, A.M., Buganza Tepole, A., Gosain, A.K., Kuhl, E., 2012. Growing skin – tissue expansion in pediatric forehead reconstruction. Biomech. Mod. Mechanobiol. 11, 855–867.
Zöllner, A.M., Abilez, O.J., Böl, M., Kuhl, E., 2012. Stretching skeletal muscle: chronic muscle lengthening through sarcomerogenesis. PLoS One 7 (10), e45661.
Zöllner, A.M., Holland, M.A., Honda, K.S., Gosain, A.K., Kuhl, E. Growth on demand – reviewing the mechanobiology of stretched skin. J. Mech. Behav. Biomed. Mat., http://dx.doi.org/10.1016/j.jmbbm.2013.03.018, in press.
Zumstein, M.A., Frey, E., von Rechenberg, B., Frigg, R., Gerber, C., Meyer, D.C., 2012. Device for lengthening of a musculotendinous unit by direct continuous traction in the sheep. BMC Vet. Res. 8, 50.

Ellen Kuhl*
Departments of Mechanical Engineering, Bioengineering, and Cardiothoracic Surgery, Stanford University, Stanford, CA, USA
E-mail address: ekuhl@stanford.edu
URL: http://biomechanics.stanford.edu

1751-6161/$ - see front matter

http://dx.doi.org/10.1016/j.jmbbm.2013.10.009

*Tel.: +1 650 450 0855; fax: +1 650 725 1587.